



# Terahertz radiation from propagating acoustic phonons based on deformation potential coupling

SANG-HYUK PARK,<sup>1</sup>  SEHYUK LEE,<sup>1</sup> KUNIE ISHIOKA,<sup>2</sup>   
CHRISTOPHER J. STANTON,<sup>3</sup> CHUL-SIK KEE,<sup>4</sup>  ANDREAS BEYER,<sup>5</sup>  
ULRICH HÖFER,<sup>5</sup> WOLFGANG STOLZ,<sup>5</sup> KERSTIN VOLZ,<sup>5</sup> AND  
YOUNG-DAHL JHO<sup>1,\*</sup>

<sup>1</sup>School of Electrical Engineering and Computer Science, Gwangju Institute of Science and Technology, Gwangju 61005, Republic of Korea

<sup>2</sup>National Institute for Materials Science, Tsukuba 305-0047, Japan

<sup>3</sup>Department of Physics, University of Florida, Gainesville, FL 32611, USA

<sup>4</sup>Advanced Photonics Research Institute, Gwangju Institute of Science and Technology, Gwangju 61005, Republic of Korea

<sup>5</sup>Material Science Center and Faculty of Physics, Philipps-University, Marburg D- 35032, Germany

\*jho@gist.ac.kr

**Abstract:** We report on new THz electromagnetic emission mechanism from deformational coupling of acoustic (AC) phonons with electrons in the propagation medium of *non-polar* Si. The epicenters of the AC phonon pulses are the surface and interface of a GaP transducer layer whose thickness ( $d$ ) is varied in nanoscale from 16 to 45 nm. The propagating AC pulses locally modulate the bandgap, which in turn generates a train of electric field pulses, inducing an abrupt drift motion at the depletion edge of Si. The fairly time-delayed THz bursts, centered at different times ( $t_1^{\text{THz}}$ ,  $t_2^{\text{THz}}$ , and  $t_3^{\text{THz}}$ ), are concurrently emitted only when a series of AC pulses reach the point of the depletion edge of Si, even without any piezoelectricity. The analysis on the observed peak emission amplitudes is consistent with calculations based on the combined effects of mobile charge carrier density and AC-phonon-induced local deformation, which recapitulates the role of deformational potential coupling in THz wave emission in a formulatively distinct manner from piezoelectric counterpart.

© 2022 Optica Publishing Group under the terms of the [Optica Open Access Publishing Agreement](#)

## 1. Introduction

The emerging phononic manipulation toward nanoscale thermal engineering [1] has sparked new hope of not only enhancing the efficiency of various modern electronics [2] but also conceptualizing novel thermal apparatus [3–6]. While the contribution of optical phonons to thermal transport is generally ignored due to their short lifetime and immobility, acoustic (AC) phonons, which spectrally encompass the terahertz (THz) frequency range, govern thermal transports in crystalline solids [7]. Ever since the pioneering measurements of the coherent Brillouin oscillations in solids [8], the optoacoustic generation mechanisms of AC wavepackets have been elucidated based either on the deformation potential coupling [9] or on the piezoelectric screening [10]. Detailed investigations of the propagation dynamics have provided novel technological perspectives, including heat conduction control [11], charge transfer [12], manipulation of microscale particles [13], and the conceptualization of a phonon laser [14–17].

In consonance with the tailored emissivity of structures over the spectral ranges spreading above  $\sim 10$  THz [18,19], the conception of radiative cooling has been envisioned to be integrated into optoelectronics [20,21] chronologically after phonon thermalization according to Planck's radiation law. On the other hand, ballistic transport governs the heat transfer processes prior

to phonon thermalization. [22] In this coherent phononic regime, the relevant emission range is limited below the tens of THz prescribed by the phonon dispersion; optical phonons are momentum-allowed to couple directly with photons [23,24], whereas radiation from AC phonons requires an additional charge-mediated coupling scheme. Interestingly, AC phonons passing through polar interfaces with discrepancies in piezoelectric coefficients have been known to trigger THz electromagnetic radiation. [25–28] In clear contrast, the role of deformational electron–AC-phonon coupling on the electromagnetic radiation has not yet been investigated.

The conversion efficiency according to the optoacoustic generation mechanism has been previously described in detail. [29–32] For instance, the generation of AC phonon on the basis of deformation potential is less productive with several orders of magnitude smaller in amplitude than the piezoelectric counterpart in the pre-saturation charge density range of the photo-Dember field [32,33]. Conversely, in order to rigorously understand how each charge–AC-phonon coupling mechanism affects THz electromagnetic radiation and to devise a framework for estimating the emission amplitude, it is useful to intuitively express the underlying processes using relevant mechanism-specific parameters, as sketched in Fig. 1. THz radiation is concurrently induced by time-varying electrical currents due to the coupling of AC phonon with charges. In the case of piezoelectric coupling, near the boundary of polar material ( $z_{int}$ ) of Fig. 1(a) with difference in piezoelectric stress constant ( $e_{33,2} - e_{33,1}$ ) [34], the propagating AC wavepacket,  $\eta(z - v_{AC}t)$ , gives rise to polarization charge density. In this way, the time-varying piezoelectric polarization current [25,26] is locally induced:  $j^{PEZ}(t) = v_{AC}(e_{33,2} - e_{33,1})\eta(z - v_{AC}t)$ . In the case of deformation potential coupling, on the other hand, the AC-phonon-induced current can be produced when the mobile charges ( $\rho_e$ ) are accelerated by  $\eta(z - v_{AC}t)$  as sketched in Fig. 1(b). Particularly at  $z_w$  where the mobile charge density changes rapidly, the drift current can be formulated as:  $j^{DP}(t) = q\mu_e \int_0^\infty \rho_e(z, t) \cdot a_{cv} \frac{\partial}{\partial z} \eta(z - v_{AC}t) dz$ , where  $\mu_e$  is the electron mobility,  $q$  is the electric charge, and  $a_{cv}$  is the deformation potential constant.

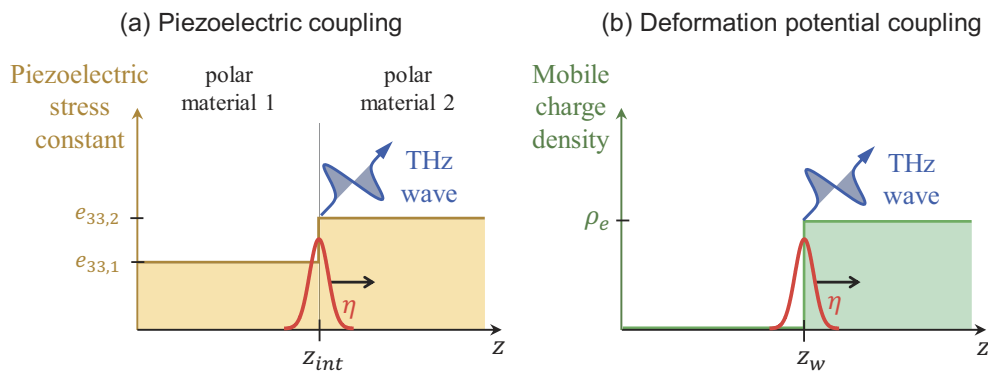


**Fig. 1.** Sketch of THz radiation induced by propagating AC wavepacket based on the mechanisms of (a) the piezoelectric coupling in polar heterointerface with different piezoelectric stress constants ( $e_{33}$ ) and (b) the deformation potential coupling with a difference in charge density ( $\rho_e$ ).

We note that deformational electron–AC-phonon coupling mechanism is ubiquitous in crystalline materials irrespective of polarity, but corresponding THz emission has been scarcely investigated possibly due to the low efficiency of acoustocurrent generation without a spatial gradient of mobile charge density. Here, we report on the deformation potential coupling scheme that produces the THz electromagnetic radiation. The emitted THz lineshapes exhibit well-defined temporal delays, matching the AC propagation routes from the epicenters to the position where electron density abruptly increases at the depletion edge of *non-polar* Si. We further show that

the THz peak amplitude is determined by the combination between the deformationally induced electric field and the electron density.

## 2. Experimental scheme

Nanoscale GaP transducers with thicknesses of  $d = 16, 35,$  and  $45$  nm were grown along non-polar (001) direction on top of a main AC propagation medium of  $n$ -type Si bulk layer. The GaP growth conditions were optimized to minimize defects according to previously reported procedures via metal-organic vapor phase epitaxy. [35,36] For above-the-gap photo-carrier excitation, a frequency-doubled Ti:sapphire pumping beam with a center wavelength of 400 nm and a pulse-duration of 150 fs was used. Considering the optical absorption depth of GaP ( $\sim 116$  nm) and that of the Si ( $\sim 82$  nm) at 400 nm, [37] photo-carrier excitation was mostly constrained up to the point of the Si depletion region whose width,  $w$ , spans about 90 nm. Accordingly, the photoexcited carriers maintain a high density near the depletion edge so that the spatial gradient of charge density is maximized, possibly maximizing the AC phonon-induced THz emission based on the deformation potential coupling. The electromagnetic emission patterns during AC propagation were then traced based on THz time-domain spectroscopy with a photo-conductive antenna (PCA) triggered by a signaling beam at 800 nm. This dichroic method is similar to that used in our previous studies on piezoelectric materials, [27,28,40] employing the equivalent PCA (BATOP PCA-44-34-100-800-h). The pump fluence on the sample surface was approximately  $83 \mu\text{J}/\text{cm}^2$ , which was sufficient to excite photocarriers on the order of  $\sim 10^{17} \text{cm}^{-3}$  at the GaP surface and GaP/Si interface.

The generation and propagation dynamics of coherent AC phonons in GaP/Si heterostructures can be elucidated along the depth ( $\equiv z$ ). [41,42] Because of differences in doping densities between the GaP transducer ( $\sim 5 \times 10^{16} \text{cm}^{-3}$ ) and Si layer ( $\sim 10^{17} \text{cm}^{-3}$ ) as a main propagation medium, the interfacial electric fields collect electrons at the surface and holes at the GaP/Si interface as sketched in Fig. 2(a). The photoexcited electrons in the Si layer ( $\rho_e^{\text{Si}}$ ) are distributed outside the depletion region, as guided by arrow in Fig. 2(a). Correspondingly, three distinct coherent longitudinal AC phonon pulses were displacively excited by the accumulated photocarriers at the surface and the GaP/Si interface: i) one from the interface that goes into the Si side [ $\eta_1$ , sketched in thick black line in Fig. 2(b)]; ii) one from the surface that descends toward the Si side ( $\eta_2$  in red line); and iii) one from the interface that ascends toward the surface then is reflected back into the Si side ( $\eta_3$  in cyan line) with velocities ( $v_{\text{AC}}$ ) of 5.8 nm/ps and 8.4 nm/ps in the GaP and Si layers, respectively [38,39]. Considering the negligible AC impedance mismatch between Si and GaP, we can safely neglect the additional reflections of  $\eta_2$  and  $\eta_3$  at the GaP/Si interface.

Based on the deformation potential coupling, the profiles of AC phonon pulses are correlated with the material parameters:  $\eta(z) \equiv \eta_{zz} = a_{\text{cv}} \cdot s_{11} \cdot \rho(z)$ . Here,  $a_{\text{cv}}$  denotes the relative deformation potential constant which is defined as the difference between the deformation potential constants of the conduction and valence bands of each valley [41], and  $s_{11}$  represents the normal component of the compliance tensor. Consequently, polarity of  $\eta(z)$  follows the sign of  $a_{\text{cv}}$ , where the  $a_{\text{cv}}$  for Si and GaP are  $-4.52$  eV and  $2.25$  eV, respectively, as investigated in our previous studies [41,42]. Therefore,  $\eta_1$  from Si side has compressive component, while  $\eta_2$  from GaP side is tensile.  $\eta_3$  has the reversed sign of  $\eta_1$  after surface reflection, as sketched in Fig. 2(b). As  $\eta_i$  locally modulates bandgap ( $a_{\text{cv}}\eta_i$ ), a localized electric field packet ( $a_{\text{cv}} \frac{\partial \eta_i}{\partial z}$ ) is synchronously induced. According to this configuration of AC phonon generation and propagation, three acoustically induced electric pulses arrive at the electron reservoir ( $\sim d + w$ ) in chronological order. In this way, AC nanowaves can interact with the mobile charge carriers and possibly generate a series of THz bursts. As a result, the THz waveform in Fig. 2(b) is formed as a line shape of bipolar pulses corresponding to  $a_{\text{cv}} \frac{\partial \eta_i}{\partial z}$ . Note, on the other hand, that transient carrier drifts upon photo-excitation, guided by arrows in Fig. 2(a), contribute to the THz radiation in

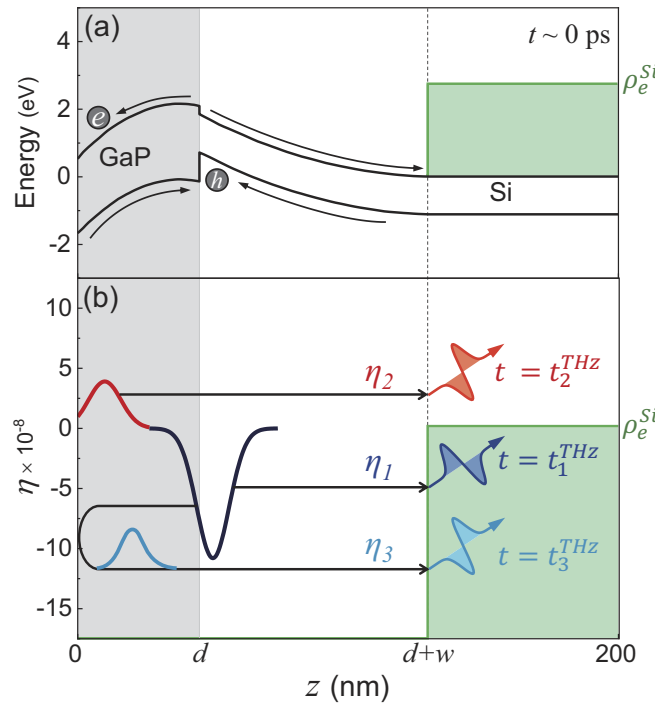


**Fig. 2.** (a) Schematic band diagram of the GaP/Si heterostructure containing photoexcited electrons and holes. The photoexcited electrons are accelerated to the surface (gray circle) or the Si-side depletion edge (green shade). Holes are accumulated at the interface (gray circle). (b) The profiles of three main AC phonon pulses  $\eta_i$  and their propagation routes. The colored oscillatory signs denote feasible THz electromagnetic emissions near  $d + w$  at different time-delays ( $t_i^{\text{THz}}$ ).

earlier time-scale and should be distinguished from the delayed reaction to AC counterparts occurring in the electron reservoir of Fig. 2(b).

### 3. Results and discussions

To investigate the correlation between the AC propagation dynamics and electromagnetic radiation, we traced the time-domain THz emission patterns with different  $d$  in Fig. 3. The temporal lineshapes in THz signals in Fig. 3(a) superimposed two distinctive oscillatory types; the contributions from the transient drift currents appear with a large amplitude near the zero time-delay ( $0 \leq t \leq 5$  ps) and those allegedly from the electron-AC-phonon coupling emerged with multiple cycles on a later timescale ( $5 < t < 45$  ps), as highlighted by the red-shaded box in Fig. 3(a) and further expanded in Fig. 3(b). The  $d$ -dependent amplitude variation of the initial THz emission near zero time-delay in Fig. 3(a) was ascribed to the competition of electrons flowing in opposite directions from the GaP/Si interface, as illustrated in top left panel of Fig. 3. [See Supplement 1 for  $d$ -dependent photo-carrier density and related THz amplitude calculation based on electric drift]. The time-delayed signals (scatters) in Fig. 3(b), on the other hand, deviated from the conventional drift-diffusion models with amplitudes less than one order of magnitude. Instead, the detailed lineshape analysis in Fig. 3(b) revealed that the three symmetrical bipolar pulses (solid lines) were superposed. We note that the amplitude of the time-delayed emission in the shades turned out to be 3 orders of magnitude smaller than our previous reports on acoustically generated THz signals at piezoelectric hetero-interfaces [28,40]

in similar experimental settings. Intriguingly enough, mechanism-specific amplitude estimation, taking into account both the optoacoustic conversion efficiency and the material parameters in Fig. 1, produced also 3 orders of magnitude smaller signal in Si in comparison to GaN/AlN hetero-interfaces. Therefore, if the time-delay also coincides with the AC propagation routes during which phonons couple with electrons, our experimental results can be considered to be related to deformational coupling in non-polar Si. Specifically, these THz waves could be emitted at the depletion edge ( $z = d + w$ ), where three propagating AC wavepackets arrive at electron reservoir with distinct time-delays, as schematized in top right panel of Fig. 3.

To account for the unfamiliar THz emission patterns of Fig. 3(b), we mathematically formulated the time-domain  $\eta$ -induced electromagnetic emission on the basis of the deformation potential coupling. Because the THz electric fields are predominantly proportional to the time derivative of the current density  $j(t)$  in far-field approximation:  $\mathcal{E}^{\text{THz}}(t) \propto \frac{\partial j(t)}{\partial t}$ , the conventional THz radiation model was first extended to encompass the  $\eta$ -induced current density of  $j^{\text{DP}}(t)$ . Then,  $j^{\text{DP}}(t)$  incorporates the continuity equation  $[\frac{\partial}{\partial t} \rho_e^{\text{Si}}(z, t) = \mu_e \frac{\partial}{\partial z} (\rho_e^{\text{Si}}(z, t) (a_{\text{cv}} \frac{\partial}{\partial z} \eta(z - v_{\text{AC}} t)))]$  and the chain rule  $[\frac{\partial}{\partial t} (a_{\text{cv}} \frac{\partial}{\partial z} \eta(z - v_{\text{AC}} t)) = -v_{\text{AC}} \frac{\partial}{\partial z} (a_{\text{cv}} \frac{\partial}{\partial z} \eta(z - v_{\text{AC}} t))]$ :

$$\begin{aligned} \mathcal{E}^{\text{THz}}(t) \propto & \mu_e \int_0^\infty \left( \frac{\partial}{\partial z} \rho_e^{\text{Si}}(z, t) \right) \left[ a_{\text{cv}} \frac{\partial}{\partial z} \eta(z - v_{\text{AC}} t) \right]^2 dz \\ & + \frac{\mu_e}{2} \int_0^\infty \rho_e^{\text{Si}}(z, t) \left( \frac{\partial}{\partial z} \left[ a_{\text{cv}} \frac{\partial}{\partial z} \eta(z - v_{\text{AC}} t) \right] \right)^2 dz \\ & - v_{\text{AC}} \int_0^\infty \rho_e^{\text{Si}}(z, t) \left( a_{\text{cv}} \frac{\partial^2}{\partial z^2} \eta(z - v_{\text{AC}} t) \right) dz. \end{aligned} \quad (1)$$

In our harmonic strain regime with  $\eta \ll 1$ , the second-order electric components ( $[a_{\text{cv}} \frac{\partial}{\partial z} \eta(z - v_{\text{AC}} t)]^2$ ) are negligible in Eq. (3). Furthermore, the first and second terms mutually nullify each other because these terms have equivalent lineshapes with opposite polarity. Thus, a contribution from the last term in Eq. (3) to  $\mathcal{E}^{\text{THz}}(t)$  mostly dominates the measured emission patterns which can be calculated based on the convolution between  $\rho_e^{\text{Si}}(z, t)$  and  $a_{\text{cv}} \frac{\partial^2}{\partial z^2} \eta(z - v_{\text{AC}} t)$ . Since the diffusion effect is negligible on the initial time-scale of THz bursts,  $\rho_e^{\text{Si}}$  was approximated to the product of the  $t$ -dependent spreading component and the Heaviside step-function in the vicinity of the depletion edge ( $z = d + w$ ). Accordingly,  $\mathcal{E}^{\text{THz}}(t)$ , for the convenience of analysis, can be simplified to incorporate observable parameters:  $\mathcal{E}^{\text{THz}}(t) \propto -v_{\text{AC}} \cdot \rho_e^{\text{Si}}(d + w, t) \cdot (a_{\text{cv}} \frac{\partial}{\partial z} \eta(z - v_{\text{AC}} t))$ . This equation implies that a series of consecutive electric pulses,  $a_{\text{cv}} \frac{\partial}{\partial z} \eta_i(z - v_{\text{AC}} t)$ , arriving at  $d + w$  accelerates the electrons, triggering THz bursts. Correspondingly,  $\mathcal{E}^{\text{THz}}$  follows the bipolar lineshape of  $a_{\text{cv}} \frac{\partial}{\partial z} \eta(z - v_{\text{AC}} t)$  whereas the peak amplitude of  $\mathcal{E}^{\text{THz}}$  is proportional to the product of  $\rho_e^{\text{Si}}(d + w, t)$  and the maximum value of  $a_{\text{cv}} \frac{\partial}{\partial z} \eta(z - v_{\text{AC}} t)$ .

From the viewpoint of how three main AC wavepackets interact with the electron reservoir under deformation potential coupling, THz emission features could be testified by inspecting the temporal resemblance between AC dynamics and THz lineshapes. Applying the mathematical simplification process to the propagation routes of three distinct AC nanowaves, we compared the detailed  $d$ -dependent experimental lineshapes (scatters) with fitting curves consisting of three superimposed bipolar pulses (solid lines) in Fig. 3(b). Herein, the peak amplitude ( $|A_i|$ ) and central position ( $t_i^{\text{THz}}$ ) of each transient THz burst were incorporated as fitting parameters, where the index  $i$  ( $=1, 2$  and  $3$ ) was assigned in a chronological order with three differently colored lines for a given  $d$  value. Evidently, the fitting curves matched remarkably well with the observed THz oscillations; three independent bipolar pulses stood out in the THz lineshapes, as anticipated

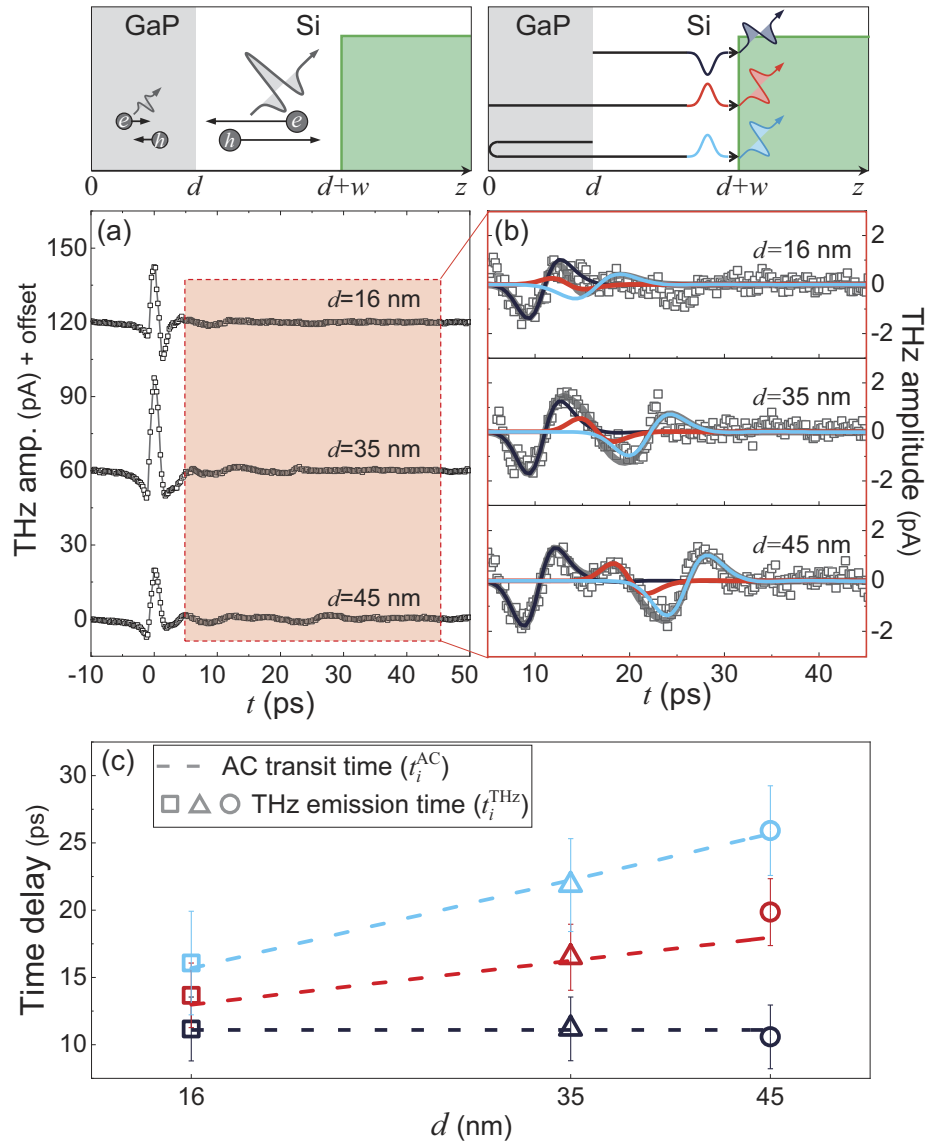


**Fig. 3.** Top panels illustrate THz radiation due to (left) the drift of photoexcited electrons from the GaP/Si interface or (right) the coupling between AC phonon and electron based on deformation potential. (a) Time-domain signal of the THz waves emitted from the GaP/Si heterostructures. (b) AC-phonon-induced THz wave signals, expanded for  $d$ -dependent propagating routes. The scattered squares represent the experimental data, and the solid lines represent the calculated curves. (c) Temporal center positions of AC-phonon-induced THz bursts for various  $d$ . The dashed lines depict the AC transit time from epicenters to the depletion edge of  $z = d + w$ .

from top right panel of Fig. 3. In this regard, we compared the  $t_i^{\text{THz}}$  extracted from Fig. 3(b) with AC transit time ( $t_i^{\text{AC}}$ ) from each epicenter to depletion edge ( $z = d + w$ ) in Fig. 3(c); the scatters show the measured  $t_i^{\text{THz}}$  values and the dashed lines correspond to  $t_i^{\text{AC}}$ . The  $t_i^{\text{AC}}$ , assigned for three distinct  $\eta_i$ , is equated as  $t_1^{\text{AC}} = w/v_{\text{AC}}^{\text{Si}}$ ,  $t_2^{\text{AC}} = w/v_{\text{AC}}^{\text{Si}} + \Delta t$ , and  $t_3^{\text{AC}} = w/v_{\text{AC}}^{\text{Si}} + 2\Delta t$ , where  $\Delta t = d/v_{\text{AC}}^{\text{GaP}}$ . The radiation times ( $t_i^{\text{THz}}$ ) agreed well with  $t_i^{\text{AC}}$ , as shown in Fig. 3(c). The earliest emission at  $t_1^{\text{THz}}$  was invariant with  $d$  since the depletion width is equal to the phonon propagation length of  $\eta_1$  in top right panel of Fig. 3. On the other hand,  $t_2^{\text{THz}}$  and  $t_3^{\text{THz}}$ , exhibited linear increment with  $d$ , in excellent agreement with the results for AC transit time around GaP layer [42].

In analogy to the way that our deformational coupling model matches the time-scale of THz emission patterns, a second line of evidence comes from examining the amplitude of THz pulse trains in terms of AC dynamics. Experimentally measured  $|A_i|$  turned out to be changing complicatedly with  $t_i^{\text{THz}}$  in Fig. 3(b). We find, however, that  $|A_i|$  can be elucidated in terms of combined contributions from  $\rho_e^{\text{Si}}(d + w, t)$  and  $a_{\text{cv}} \frac{\partial}{\partial z} \eta_i$ :  $|A_i| \propto v_{\text{AC}} \cdot \rho_e^{\text{Si}}(d + w, t) \cdot \max\{|a_{\text{cv}} \frac{\partial}{\partial z} \eta_i|\}$ . In this regard, we separately calculated  $\rho_e^{\text{Si}}(d + w, t)$  and  $\max\{|a_{\text{cv}} \frac{\partial}{\partial z} \eta_i|\}$  as a function of  $d$ , then compared the calculations of  $|A_i|$  with the measurements in Fig. 4. Firstly, we calculated the spatio-temporal profile of  $\rho_e^{\text{Si}}$  from 10 ps to 30 ps with an interval of 5 ps in Fig. 4(a). The photoexcited electrons and holes tend to diffuse at different speeds towards the + $z$ -direction, while the electronic diffusion particularly near  $z = d + w$  is disturbed by the strong attractive interaction with the holes [43] accumulated at  $z \sim d$ ; hence,  $\rho_e^{\text{Si}}$  remains large at  $z = d + w$  in the early time range of <30 ps, whereas the profile in the interior of Si layer deviates from the step-function. The influence of such deviation on the emitted THz lineshape, however, is negligibly small because the spatial decay-length of  $\rho_e^{\text{Si}}$  [>200 nm at 30 ps in Fig. 4(a)] is much larger than the spatial-width of the wavepackets  $\sim 15$  nm (See Sec. 3 and 4 of the Supplement 1 for details on the carrier density profiles based on the drift-diffusion transport equation and the THz lineshape calculations using the realistic profiles of  $\rho_e^{\text{Si}}$ , respectively). The value of  $\rho_e^{\text{Si}}$  at  $z = d + w$  was then extracted as a function of time by a green line in the inset of Fig. 4(a). The  $\rho_e^{\text{Si}}(d + w, t)$  increases slightly from  $6 \times 10^{15} \text{ cm}^{-3}$  to  $6.5 \times 10^{15} \text{ cm}^{-3}$  within the time-scale of  $10 < t < 25$  ps, which encompassed the range of  $t_i^{\text{THz}}$  for different  $d$  as denoted by different scatters along the green line.

As a key factor to determine  $|A_i|$ ,  $\max\{|a_{\text{cv}} \frac{\partial}{\partial z} \eta_i|\}$  was calculated as a function of  $d$ , considering the photo-carrier densities and the associated material parameter of  $a_{\text{cv}}$  based on the deformation potential coupling model.  $a_{\text{cv}}$  of Si (−4.52 eV) contributing to the value of  $\max\{|a_{\text{cv}} \frac{\partial}{\partial z} \eta_1|\}$  was much larger than the  $a_{\text{cv}}$  for GaP (2.25 eV) involved in  $\max\{|a_{\text{cv}} \frac{\partial}{\partial z} \eta_2|\}$ . Meanwhile, the accumulated hole density in correlation with  $\max\{|a_{\text{cv}} \frac{\partial}{\partial z} \eta_1|\}$  was  $\sim 2$  times larger than the accumulated electron density with respect to  $\max\{|a_{\text{cv}} \frac{\partial}{\partial z} \eta_2|\}$ , because the holes are collected near the interface from the both surrounding layers of GaP and Si [cf. Figure 2(a)]. According to the values of  $a_{\text{cv}}$  and the  $d$ -dependent accumulated carrier densities,  $\max\{|a_{\text{cv}} \frac{\partial}{\partial z} \eta_i|\}$  were estimated as a function of  $d$  in Fig. 4(b). We clearly see that  $\max\{|a_{\text{cv}} \frac{\partial}{\partial z} \eta_1|\}$  is larger than  $\max\{|a_{\text{cv}} \frac{\partial}{\partial z} \eta_2|\}$  by  $\sim 4$  times. The increasing trend of  $\max\{|a_{\text{cv}} \frac{\partial}{\partial z} \eta_1|\}$  and  $\max\{|a_{\text{cv}} \frac{\partial}{\partial z} \eta_2|\}$  originated from the cumulative carrier densities increasing with  $d$ .

By incorporating the distinct  $d$ -dependencies of  $\rho_e^{\text{Si}}(d + w, t)$  and increasing  $\max\{|a_{\text{cv}} \frac{\partial}{\partial z} \eta_i|\}$ ,  $|A_i|$  can be quantified in Fig. 4(c). The scatters are the experimental results extracted from Fig. 3(b), whereas dashed lines are calculated from the product of the results in Fig. 4(a) and Fig. 4(b). Considering the rather stagnant  $\rho_e^{\text{Si}}(d + w, t)$  in the inset of Fig. 4(a),  $|A_i|$  followed decisively  $\max\{|a_{\text{cv}} \frac{\partial}{\partial z} \eta_i|\}$  variation. In compliance with the difference in values between  $\max\{|a_{\text{cv}} \frac{\partial}{\partial z} \eta_1|\}$  and  $\max\{|a_{\text{cv}} \frac{\partial}{\partial z} \eta_2|\}$ ,  $|A_1|$  exhibits  $\sim 4$  times larger values than those of  $|A_2|$ . Similarly, the increasing tendency of  $|A_1|$  and  $|A_2|$  with  $d$  resulted from the increasing  $\max\{|a_{\text{cv}} \frac{\partial}{\partial z} \eta_i|\}$  with  $d$ .

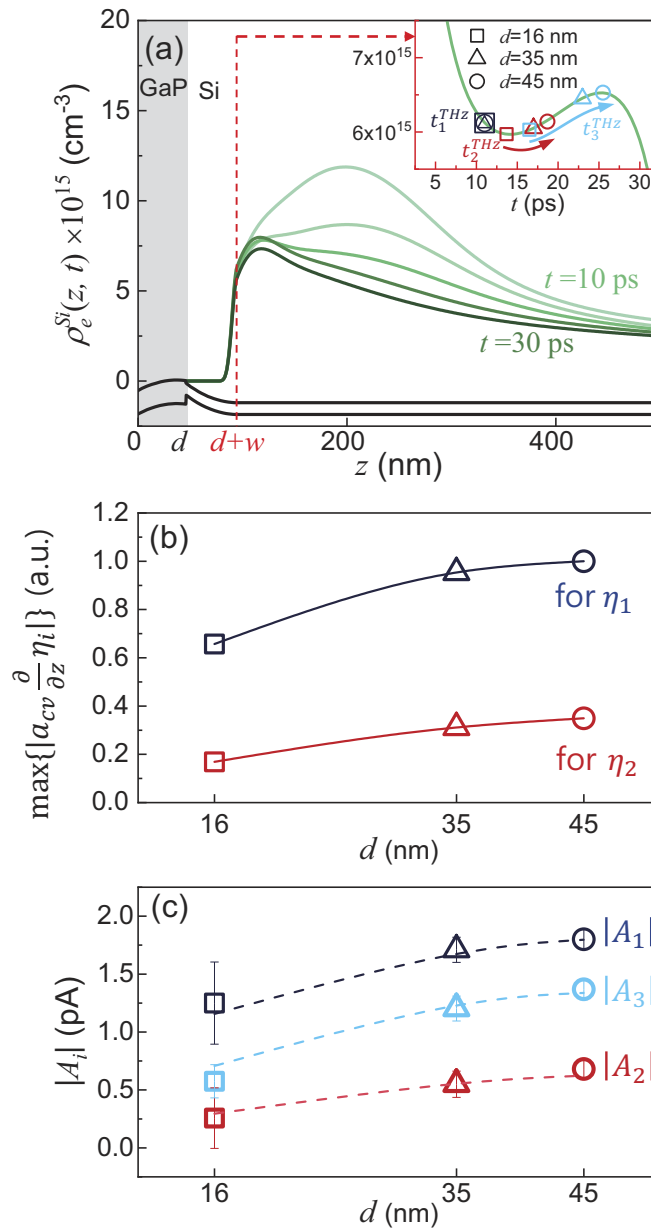


**Fig. 4.** (a) Spatio-temporal profile of the photoexcited electron density in the Si layer ( $\rho_e^{Si}$ ). Inset shows  $\rho_e^{Si}$  as a function of time at the depletion edge ( $z = d + w$ ) indicated by the red dashed line in (a). Different symbols in inset indicate the THz radiation times related to the increasing  $d$  represented by the right arrows. (b) Peak amplitude of AC-phonon-induced electric field  $a_{cv} \frac{\partial}{\partial z} \eta$  as a function of  $d$ . (c) Comparison of the measured (scattered lines) and calculated (dashed lines) amplitudes of the THz waves ( $|A_i|$ ) for different  $d$ .

In this way, the intuitively calculated  $|A_1|$  and  $|A_2|$  corresponded quantitatively with the measured values.

Finally, we analyzed the variation of  $|A_3|$  in comparison with  $|A_1|$ . Since  $\eta_1$  and  $\eta_3$  correspond to AC wavepackets that oppositely propagate from the same epicenter of the GaP/Si interface [cf. Figure 2(b)],  $|A_3|$  could remain the same with  $|A_1|$  under total reflection at the atomically flat surface. However, the observed values of  $|A_3|$  declined severely from those of  $|A_1|$  in Fig. 4(c). The decrease of  $|A_3|$  from  $|A_1|$  evidently indicates the role of AC attenuation during the diffuse surface scattering of  $\eta_3$ . Such amplitude reduction at the surface has been well-associated with the diffuse Kapitza scattering in terms of the specularly parameter [44], where the affiliated AC wavelength is comparable to or smaller than surface roughness ( $\delta$ ). In this regard, the  $\delta$  was quantified by atomic force microscopy to be about 2.1, 1.6, and 1.4 nm for the samples with  $d = 16, 35, \text{ and } 45$  nm, respectively. Using the measured  $\delta$ , the attenuation of  $\eta_3$  was evaluated by incorporating the frequency-dependent diffuse Kapitza scattering of each Fourier component. Consequently, the amplitude attenuation of  $\eta_3$  in comparison to  $\eta_1$  (thus without surface scattering) was estimated to be 42%, 31%, and 29% for the samples with different  $d$  values of 16, 35, and 45 nm, respectively (The detailed procedures for estimating the diffuse Kapitza scattering are provided in Sec. 5 of Supplement 1). The calculated values of  $|A_3|$  in line with such surface scattering (blue dashed lines) matched well with measured values (scatters) in Fig. 4(c).

To investigate the spectrum of AC-phonon-induced THz emission, the Eq. (3) can be further modified by simplifying  $\rho_e^{\text{Si}}(z, t)$ . As can be seen in Fig. 4(a), the temporal change of  $\rho_e^{\text{Si}}$  near  $z = d + w$  is very small. Accordingly, the last term in Eq. (3) can be expressed in terms of convolution as  $\mathcal{E}^{\text{THz}}(t) \propto -v_{\text{AC}} \int_0^\infty \rho_e^{\text{Si}}(z) \left( a_{\text{cv}} \frac{\partial^2}{\partial z^2} \eta(z - v_{\text{AC}}t) \right) dz \sim -v_{\text{AC}} \left\{ \rho_e^{\text{Si}}(v_{\text{AC}}t) * \left( a_{\text{cv}} \frac{\partial^2}{\partial z^2} \eta(v_{\text{AC}}t) \right) \right\}$ . In this way, the Fourier-transform of  $\mathcal{E}^{\text{THz}}$  can be obtained as:  $\mathcal{F}[\mathcal{E}^{\text{THz}}(t)] \propto \mathcal{F}[\rho_e^{\text{Si}}(v_{\text{AC}}t)] \cdot \mathcal{F}\left[ a_{\text{cv}} \frac{\partial^2}{\partial z^2} \eta(v_{\text{AC}}t) \right]$ . We compared the spectrum of measured  $\mathcal{E}^{\text{THz}}$  (scatters) to the calculation (black solid line) as shown in Fig. 5. The separate spectral components of  $\mathcal{F}[\rho_e^{\text{Si}}(v_{\text{AC}}t)]$  and  $\mathcal{F}\left[ a_{\text{cv}} \frac{\partial^2}{\partial z^2} \eta(v_{\text{AC}}t) \right]$  were estimated, as displayed in the inset of Fig. 5.  $\mathcal{F}\left[ a_{\text{cv}} \frac{\partial^2}{\partial z^2} \eta(v_{\text{AC}}t) \right]$  has a peak frequency of  $\sim 135$  GHz and full width at half maximum (FWHM) of  $\sim 156$  GHz, while the calculated  $\mathcal{F}[\mathcal{E}^{\text{THz}}(t)]$  has a lower peak frequency of  $\sim 100$  GHz. This spectral shift was caused by the combination of low-frequency components of  $\mathcal{F}[\rho_e^{\text{Si}}(v_{\text{AC}}t)]$  that occurred with a spatially wide profile. The measured spectrum of  $\mathcal{E}^{\text{THz}}$  shows a lower peak frequency compared to the calculated  $\mathcal{F}[\mathcal{E}^{\text{THz}}(t)]$ . These spectral differences can be attributed to spectral attenuation during AC propagation such as phonon-phonon scattering [45,46], boundary scatterings [47], and electron-phonon scattering [48]. Such scattering-induced spectral attenuation can be further investigated by quantitatively analyzing the spectrum of  $\mathcal{E}^{\text{THz}}$ . However, detailed consideration of this spectral attenuation during AC propagation is beyond the scope of this work and will be discussed elsewhere.

The previously reported transient electrical current by AC-phonon–electron coupling based on the deformation potential implies that the THz emission may also be produced by the deformational AC-phonon-electron coupling. [49] However, the lack of analytical modeling made it difficult to specify the required material parameters and experimental conditions. Intuitively, the electron density gradient and amplitude of AC wavepacket are the key factors in generating the AC-phonon–induced transient current density. Furthermore, the amplitude of  $\mathcal{E}^{\text{THz}}$  is proportional to the second-order spatial derivative of  $\eta$  based on our formulation, indicating that a narrower spatial width of  $\eta$  can enhance the THz amplitude. Indeed, we could observe the AC-phonon–induced THz emission features by generating the nanoscale wavepackets with spatial width of  $\sim 15$  nm. In this context, such mathematical modeling can be useful to understand the

contribution of each factor to THz emission, such as spatial phonon distribution and  $\rho_e$  gradient, and thus increase the AC-phonon induced THz emission amplitude.

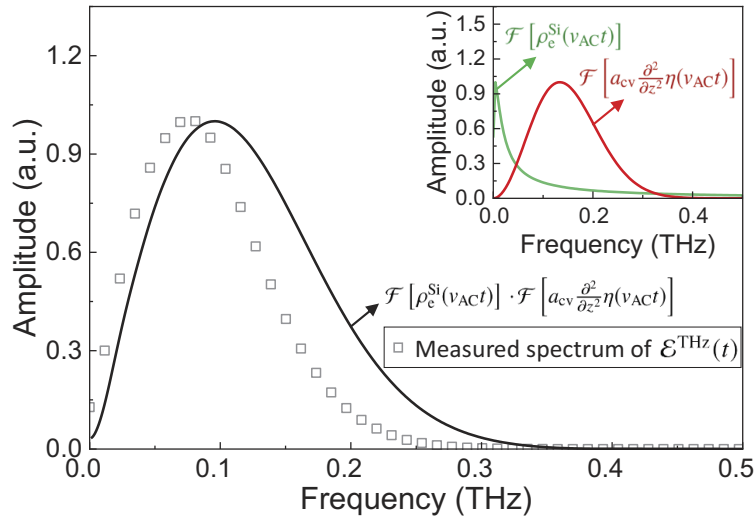


**Fig. 5.** Spectral comparison between measurement (scatters) and calculation (black solid line) of AC-phonon-induced THz wave ( $\mathcal{F}[\mathcal{E}^{\text{THz}}(t)]$ ). Inset shows spectra of photoexcited electron distribution ( $\mathcal{F}[\rho_e^{\text{Si}}(v_{\text{AC}}t)]$ ) and spatial derivative of AC-phonon-induced electric field ( $\mathcal{F}[a_{\text{cv}} \frac{\partial^2}{\partial z^2} \eta(v_{\text{AC}}t)]$ ).

#### 4. Conclusion

We experimentally demonstrated that the deformational coupling between AC nanowaves and mobile electrons contributes to THz electromagnetic radiation in a non-polar material, wherein a clear temporal response has been found to be associated with AC dynamics. The time-delayed lineshapes, dependent on various AC propagation paths from the nanoscale epicenters to the point of strongest charge modulation in the electron reservoir, contrasted with those from the charge carrier drift upon excitation. Additional dependency of THz peak amplitude on the product of electron density at the depletion edge and AC-phonon-induced electric field was further understood through the AC-phonon-electron coupling under the deformation potential, which was distinguished from the well-known effect of interfacial coupling provoked with different piezoelectric coefficients. Our observations and modeling of THz emission during AC propagation in non-polar crystals demonstrate that deformational coupling, previously known to affect only the phonon generation processes, also induces electromagnetic radiation.

**Funding.** Korea Electric Power Corporation (R17XA05-64); National Research Foundation of Korea (2018R1A2B6008101); Ministry of Education (2021R111A2059710); Deutsche Forschungsgemeinschaft (Project-ID 223848855-SFB 1083); Air Force Office of Scientific Research (FA9550-17-1-0341).

**Disclosures.** The authors declare no conflicts of interest.

**Data availability.** Data underlying the results presented in this paper are not publicly available at this time but may be obtained from the authors upon reasonable request.

**Supplemental document.** See [Supplement 1](#) for supporting content.

#### References

1. D. G. Cahill, P. V. Braun, G. Chen, D. R. Clarke, S. Fan, K. E. Goodson, P. Keblinski, W. P. King, G. D. Mahan, A. Majumdar, H. J. Maris, S. R. Phillpot, E. Pop, and L. Shi, "Nanoscale thermal transport. II. 2003–2012," *Appl. Phys. Rev.* **1**(1), 011305 (2014).

2. J. Schlee, J. Mateos, I. Íñiguez-de-la-Torre, N. Wadefalk, P. A. Nilsson, J. Grahn, and A. J. Minnich, "Phonon black-body radiation limit for heat dissipation in electronics," *Nat. Mater.* **14**(2), 187–192 (2015).
3. J. Mao, G. Chen, and Z. Ren, "Thermoelectric cooling materials," *Nat. Mater.* **20**(4), 454–461 (2021).
4. G. Wehmeyer, T. Yabuki, C. Monachon, J. Wu, and C. Dames, "Thermal diodes, regulators, and switches: Physical mechanisms and potential applications," *Appl. Phys. Rev.* **4**(4), 041304 (2017).
5. N. Yazdani, M. Jansen, D. Bozyigit, W. M. M. Lin, S. Volk, O. Yarema, M. Yarema, F. Juranyi, S. D. Huber, and V. Wood, "Nanocrystal superlattices as phonon-engineered solids and acoustic metamaterials," *Nat. Commun.* **10**(1), 4236 (2019).
6. B. Sun, S. Niu, R. P. Hermann, J. Moon, N. Shulumba, K. Page, B. Zhao, A. S. Thind, K. Mahalingam, J. Milam-Guerrero, R. Haiges, M. Mecklenburg, B. C. Melot, Y. D. Jho, B. M. Howe, R. Mishra, A. Alatas, B. Winn, M. E. Manley, J. Ravichandran, and A. J. Minnich, "High frequency atomic tunneling yields ultralow and glass-like thermal conductivity in chalcogenide single crystals," *Nat. Commun.* **11**(1), 6039 (2020).
7. X. Wang and B. Huang, "Computational study of in-plane phonon transport in Si thin films," *Sci. Rep.* **4**(1), 6399 (2014).
8. C. Thomsen, H. T. Grahn, H. J. Maris, J. Tauc, and J. J. Hauser, "Coherent phonon generation and detection by picosecond light pulses," *Phys. Rev. Lett.* **53**(10), 989–992 (1984).
9. O. B. Wright and K. Kawashima, "Coherent phonon detection from ultrafast surface vibrations," *Phys. Rev. Lett.* **69**(11), 1668–1671 (1992).
10. C. K. Sun, J. C. Liang, and X.-Y. Yu, "Coherent acoustic phonon oscillations in semiconductor multiple quantum wells with piezoelectric fields," *Phys. Rev. Lett.* **84**(1), 179–182 (2000).
11. G. Pernot, M. Stoffel, I. Savic, F. Pezzoli, P. Chen, G. Savelli, A. Jacquot, J. Schumann, U. Denker, I. Mönch, Ch. Deneke, O. G. Schmidt, J. M. Rampnoux, S. Wang, M. Plissonnier, A. Rastelli, S. Dilhaire, and N. Mingo, "Precise control of thermal conductivity at the nanoscale through individual phonon-scattering barriers," *Nat. Mater.* **9**(6), 491–495 (2010).
12. E. S. K. Young, A. V. Akimov, M. Henini, L. Eaves, and A. J. Kent, "Subterahertz acoustical pumping of electronic charge in a resonant tunneling device," *Phys. Rev. Lett.* **108**(22), 226601 (2012).
13. Z. Wang and J. Zhe, "Recent advances in particle and droplet manipulation for lab-on-a-chip devices based on surface acoustic waves," *Lab Chip* **11**(7), 1280–1285 (2011).
14. I. S. Grudinin, H. Lee, O. Painter, and K. J. Vahala, "Phonon laser action in a tunable two-level system," *Phys. Rev. Lett.* **104**(8), 083901 (2010).
15. R. P. Beardsley, A. V. Akimov, M. Henini, and A. J. Kent, "Coherent terahertz sound amplification and spectral line narrowing in a stark ladder superlattice," *Phys. Rev. Lett.* **104**(8), 085501 (2010).
16. A. Fainstein, N. D. Lanzillotti-Kimura, B. Jusserand, and B. Perrin, "Strong optical-mechanical coupling in a vertical GaAs/AlAs microcavity for subterahertz phonons and near-infrared light," *Phys. Rev. Lett.* **110**(3), 037403 (2013).
17. I. Mahboob, K. Nishiguchi, A. Fujiwara, and H. Yamaguchi, "Phonon lasing in an electromechanical resonator," *Phys. Rev. Lett.* **110**(12), 127202 (2013).
18. S. Fan and W. Li, "Photonics and thermodynamics concepts in radiative cooling," *Nat. Photonics* **16**(3), 182–190 (2022).
19. J. Xu, J. Mandal, and A. P. Raman, "Broadband directional control of thermal emission," *Science* **372**(6540), 393–397 (2021).
20. Y. An, C. Sheng, and X. Li, "Radiative cooling of solar cells: opto-electro-thermal physics and modeling," *Nanoscale* **11**(36), 17073–17083 (2019).
21. T. Sadi, I. Radevici, and J. Oksanen, "Thermophotonic cooling with light-emitting diodes," *Nat. Photonics* **14**(4), 205–214 (2020).
22. G. Varnavides, A. S. Jermyn, P. Anikeeva, and P. Narang, "Nonequilibrium phonon transport across nanoscale interfaces," *Phys. Rev. B* **100**(11), 115402 (2019).
23. M. Tani, R. Fukasawa, H. Abe, S. Matsuura, and K. Sakai, "Terahertz radiation from coherent phonons excited in semiconductors," *J. Appl. Phys.* **83**(5), 2473–2477 (1998).
24. T. Dekorsy, H. Auer, H. J. Bakker, H. G. Roskos, and H. Kurz, "THz electromagnetic emission by coherent infrared-active phonons," *Phys. Rev. B* **53**(7), 4005–4014 (1996).
25. E. J. Reed, M. R. Armstrong, K. Y. Kim, and J. H. Glowia, "Atomic-scale time and space resolution of terahertz frequency acoustic waves," *Phys. Rev. Lett.* **101**(1), 014302 (2008).
26. M. R. Armstrong, E. J. Reed, K. Y. Kim, J. H. Glowia, W. M. Howard, E. L. Piner, and J. C. Roberts, "Observation of terahertz radiation coherently generated by acoustic waves," *Nat. Phys.* **5**(4), 285–288 (2009).
27. C. J. Stanton, G. D. Sanders, R. Liu, G. W. Chern, C. K. Sun, J. S. Yahng, Y. D. Jho, J. Y. Sohn, E. Oh, and D. S. Kim, "Coherent phonons, nanoseismology and THz radiation in InGaN/GaN heterostructures," *Superlattices Microstruct.* **34**(3-6), 525–529 (2003).
28. H. Jeong, Y. D. Jho, and C. J. Stanton, "Electrical manipulation of crystal symmetry for switching transverse acoustic phonons," *Phys. Rev. Lett.* **114**(4), 043603 (2015).
29. D. M. Moss, A. V. Akimov, A. J. Kent, B. A. Glavin, M. J. Kappers, J. L. Hollander, M. A. Moram, and C. J. Humphreys, "Coherent terahertz acoustic vibrations in polar and semipolar gallium nitride-based superlattices," *Appl. Phys. Lett.* **94**(1), 011909 (2009).

30. P. Babilotte, P. Ruello, T. Pezeril, G. Vaudel, D. Mounier, J.-M. Breteau, and V. Gusev, "Transition from piezoelectric to deformation potential mechanism of hypersound photogeneration in *n*-doped GaAs semiconductors," *J. Appl. Phys.* **109**(6), 064909 (2011).
31. Y.-C. Wen, "Efficient generation of coherent acoustic phonons in (111) InGaAs/GaAs multiple quantum wells through piezoelectric effects," *Appl. Phys. Lett.* **90**(17), 172102 (2007).
32. G. Vaudel, T. Pezeril, A. Lomonosov, M. Lejman, P. Ruello, and V. Gusev, "Laser generation of hypersound by a terahertz photo-Dember electric field in a piezoelectric GaAs semiconductor," *Phys. Rev. B* **90**(1), 014302 (2014).
33. P. Ruello and V. E. Gusev, "Physical mechanisms of coherent acoustic phonons generation by ultrafast laser action," *Ultrasonics* **56**, 21–35 (2015).
34. E. T. Yu, X. Z. Dang, P. M. Asbeck, and S. S. Lau, "Spontaneous and piezoelectric polarization effects in III–V nitride heterostructures," *J. Vac. Sci. Technol. B* **17**(4), 1742 (1999).
35. A. Beyer, J. Ohlmann, S. Liebich, H. Heim, G. Witte, W. Stolz, and K. Volz, "GaP heteroepitaxy on Si (001): Correlation of Si-surface structure, GaP growth conditions, and Si-III/V interface structure," *J. Appl. Phys.* **111**(8), 083534 (2012).
36. A. Beyer, A. Stegmüller, J. Oelerich, K. Jandieri, K. Werner, G. Mette, W. Stolz, S. D. Baranovskii, R. Tonner, and K. Volz, "Pyramidal structure formation at the interface between III/V semiconductors and silicon," *Chem. Mater.* **28**(10), 3265–3275 (2016).
37. D. E. Aspnes and A. A. Studna, "Dielectric functions and optical parameters of Si, Ge, GaP, GaAs, GaSb, InP, InAs, and InSb from 1.5 to 6.0 eV," *Phys. Rev. B* **27**(2), 985–1009 (1983).
38. R. Weil and W. O. Groves, "The elastic constants of gallium phosphide," *J. Appl. Phys.* **39**(9), 4049–4051 (1968).
39. H. J. McSkimin and P. Andreatch Jr., "Elastic moduli of silicon vs hydrostatic pressure at 25.0 °C and -195.8 °C," *J. Appl. Phys.* **35**(7), 2161–2165 (1964).
40. H. Jeong, Y. D. Jho, S. H. Rhim, K. J. Yee, S. Y. Yoon, J. P. Shim, D. S. Lee, J. W. Ju, J. H. Baek, and C. J. Stanton, "Electrical modulation and switching of transverse acoustic phonons," *Phys. Rev. B* **94**(2), 024307 (2016).
41. K. Ishioka, A. Rustagi, A. Beyer, W. Stolz, K. Volz, U. Höfer, H. Petek, and C. J. Stanton, "Sub-picosecond acoustic pulses at buried GaP/Si interfaces," *Appl. Phys. Lett.* **111**(6), 062105 (2017).
42. K. Ishioka, A. Beyer, W. Stolz, K. Volz, H. Petek, U. Höfer, and C. J. Stanton, "Coherent optical and acoustic phonons generated at lattice-matched GaP/Si (0 0 1) heterointerfaces," *J. Phys.: Condens. Matter* **31**, 094003 (2019).
43. M. M. Gabriel, E. M. Grumstrup, J. R. Kirschbrown, C. W. Pinion, J. D. Christesen, D. F. Zigler, E. E. M. Cating, J. F. Cahoon, and J. M. Papanikolas, "Imaging charge separation and carrier recombination in nanowire pin junctions using ultrafast microscopy," *Nano Lett.* **14**(6), 3079–3087 (2014).
44. J. M. Ziman, *Electrons and Phonons: The Theory of Transport Phenomena in Solids* (Oxford University Press, Oxford, UK, 1960).
45. D. G. Cahill, F. Watanabe, A. Rockett, and C. B. Vining, "Thermal conductivity of epitaxial layers of dilute SiGe alloys," *Phys. Rev. B* **71**(23), 235202 (2005).
46. B. C. Daly, K. Kang, Y. Wang, and David G. Cahill, "Picosecond ultrasonic measurements of attenuation of longitudinal acoustic phonons in silicon," *Phys. Rev. B* **80**(17), 174112 (2009).
47. Y. C. Wen, C. L. Hsieh, K. H. Lin, H. P. Chen, S. C. Chin, C. L. Hsiao, Y. T. Lin, C. S. Chang, Y. C. Chang, L. W. Tu, and C. K. Sun, "Specular Scattering Probability of Acoustic Phonons in Atomically Flat Interfaces," *Phys. Rev. Lett.* **103**(26), 264301 (2009).
48. B. Liao, A. A. Maznev, K. A. Nelson, and G. Chen, "Photo-excited charge carriers suppress sub-terahertz phonon mode in silicon at room temperature," *Nat. Commun.* **7**(1), 13174 (2016).
49. D. M. Moss, A. V. Akimov, B. A. Glavin, M. Henini, and A. J. Kent, "Ultrafast Strain-Induced Current in a GaAs Schottky Diode," *Phys. Rev. Lett.* **106**(6), 066602 (2011).